Diffusion Model-Enhanced Environment Reconstruction in ISAC

Nguyen Duc Minh Quang, Chang Liu, *Member, IEEE*, Shuangyang Li, *Member, IEEE*, Hoai-Nam Vu, Derrick Wing Kwan Ng, *Fellow, IEEE*, Wei Xiang, *Senior Member, IEEE*

Abstract—Recently, environment reconstruction (ER) in integrated sensing and communication (ISAC) systems has emerged as a promising approach for achieving high-resolution environmental perception. However, the initial results obtained from ISAC systems are coarse and often unsatisfactory due to the high sparsity of the point clouds and significant noise variance. To address this problem, we propose a noise–sparsity-aware diffusion model (NSADM) post-processing framework. Leveraging the powerful data recovery capabilities of diffusion models, the proposed scheme exploits spatial features and the additive nature of noise to enhance point cloud density and denoise the initial input. Simulation results demonstrate that the proposed method significantly outperforms existing model-based and deep learning-based approaches in terms of Chamfer distance and root mean square error.

Index Terms—Environment reconstruction, deep learning, diffusion models, integrated sensing and communication.

I. Introduction

Environment reconstruction (ER) is a key enabler for critical applications such as autonomous navigation, smart-city monitoring [1]. To support these applications, Integrated Sensing and Communication (ISAC) [2] has emerged as a promising technology for future 6G networks, unifying sensing and communication capabilities within a single system design [3]-[5]. By leveraging ISAC, ER can be realized by processing the received echoes to estimate the locations of reflection points, each corresponding to a detected object surface in a specific direction. Aggregating these reflections yields a point cloud representing the surroundings without requiring dedicated sensing hardware. Despite its potential, ISAC-enabled ER faces significant challenges, such as limited bandwidth and low received signal-to-noise ratio (SNR). Consequently, the ISAC-enabled point clouds often suffer from missed detections and high noise variance, resulting in a significant decline in ER performance. Thus, the post-processing of ISAC-enabled point clouds plays a critical role in ER, garnering significant attention from both academia and industry [2].

Recent research has explored post-processing techniques to enhance ISAC-enabled ER in terms of accuracy and density. For instance, Bazzi et al. [6] extract multipath components from channel state information and develop a two-stage reflection point optimization algorithm for 3D ER. In another direction, Lin et al. [7] introduce a framework that uses

N. D. M. Quang, C. Liu, and W. Xiang are with the School of Computing, Engineering, and Mathematical Sciences, La Trobe University, Melbourne, VIC 3086, Australia (e-mail: quang.nguyen@latrobe.edu.au; c.liu6@latrobe.edu.au; w.xiang@latrobe.edu.au).

S. Li is with the Chair of Communications and Information Theory, Technical University of Berlin, 10623 Berlin, Germany (e-mail: shuangyang.li@tuberlin.de).

H.-N. Vu is with the Faculty of Artificial Intelligence, Posts and Telecommunications Institute of Technology, Hanoi 12110, Vietnam (e-mail: namvh@ptit.edu.vn).

D. W. K. Ng is with the School of Electrical Engineering and Telecommunications, University of New South Wales, Sydney, NSW 2052, Australia (e-mail: w.k.ng@unsw.edu.au).

uplink signals from multiple users, along with a user selection algorithm, to improve the precision of the reflection point estimation. As an alternative, deep learning approaches have shown promise in ISAC [8], [9]. For example, Lu et al. [10] present a deep learning-based pipeline that employs two neural networks for 4D environmental reconstruction, significantly improving the density and structural coherence of the output point clouds. Despite their acceptable performance, these aforementioned methods tend to focus exclusively on either mitigating point cloud sparsity or suppressing additive noise, while in practice, both issues often coexist.

Recently, diffusion models have demonstrated strong data recovery capabilities across various domains [11]. Notably, diffusion models possess inherent denoising and generative capabilities, making them highly effective for point cloud refinement. Motivated by these strengths, this letter proposes a diffusion model-based approach to enhance ER in ISAC systems. First, we formulate a generalized point cloud estimation problem for ISAC-enabled ER that jointly accounts for range estimation noise and missed detections by incorporating CRB-based noise variance and detection probability modeling to capture the statistical characteristics of ISAC point clouds. Second, we propose a noise-sparsity-aware diffusion model (NSADM) framework, where the forward process integrates CRB-guided noise injection and sparsity simulation to emulate realistic ISAC degradation. In the reverse process, the denoising network is conditioned on the CRB-based noise variance and detection probability matrices, leading to improved denoising and densification performance. Finally, extensive simulations demonstrate that the proposed method significantly improves both qualitative reconstruction and quantitative metrics, achieving lower Chamfer Distance and RMSE than existing model-based and learning-based baselines.

II. SYSTEM MODEL AND PROBLEM FORMULATION

As illustrated in Fig. 1, we consider a downlink ISAC scenario in which a base station (BS) transmits ISAC signals and collects reflected echoes from multiple static objects to conduct the task of ER. The BS is equipped with a square uniform planar array (UPA) consisting of $N_t \times N_t$ transmit and $N_r \times N_r$ receive antennas.

A. Signal Model

Let $s_n(t)$ denote the transmitted symbol at time instant t in the nth time slot, with total transmit power P_s . The BS transmits

$$\mathbf{x}_n(t) = \mathbf{w}_n s_n(t),\tag{1}$$

where \mathbf{w}_n is the transmit beamforming vector. The beamforming vector is selected from a predefined codebook $\mathcal{B} = \{\mathbf{a}(\phi_i,\theta_j) \mid \phi_i \in \Phi, \; \theta_j \in \Theta\}$ [7], where $\Phi = \{\phi_1,\ldots,\phi_W\}$ and $\Theta = \{\theta_1,\ldots,\theta_H\}$ denote the discrete sets of azimuth and elevation angles, with W and H representing the total number

(7)



Fig. 1: An illustration of the ISAC ER scenario.

of azimuth and elevation grid points, respectively. At each time slot, the BS sets $\mathbf{w}_n = \mathbf{a}(\phi_i, \theta_j)$, where $\mathbf{a}(\phi_i, \theta_j) \in \mathbb{C}^{N_t^2}$ is the steering vector toward direction (ϕ_i, θ_j) . For a square UPA with $N_t \times N_t$ elements and half wavelength spacing, the steering vector is written as

$$\mathbf{a}(\phi_i, \theta_j) = \frac{1}{\sqrt{N_t^2}} \left[e^{j\pi(m\sin\theta_j\cos\phi_i + n\sin\theta_j\sin\phi_i)} \right]_{m,n=0}^{N_t - 1},$$
(2)

where each entry corresponds to the antenna element indexed by (m, n). Under this model, the received echo at the BS corresponding to beam direction (ϕ_i, θ_j) can be written as [4]

$$\mathbf{y}_n(t) = \sqrt{N_t^2 N_r^2} g_{i,j} \mathbf{a}(\phi_i, \theta_j) \mathbf{a}^H(\phi_i, \theta_j) s_n(t - \tau_{i,j}) + \mathbf{z}(t),$$
(3)

where $\tau_{i,j}$ is the round-trip delay and $g_{i,j} = \beta_{i,j} h_{i,j}$ denotes the dominant path gain¹. Here, $\beta_{i,j} = \frac{\varrho_{i,j}}{2d_{i,j}}$ depends on the distance $d_{i,j}$ and radar cross section (RCS) $\varrho_{i,j}$, while $h_{i,j}$ captures small-scale fading with $\mathbb{E}[|h_{i,j}|^2] = 1$. RCS depends on the static object geometry, surface material, and incidence angle, whereas motion-induced variations are not considered due to the quasi-static setup. The term $z(t) \sim \mathcal{CN}(0, \sigma_z^2 I_{N_r})$ models aggregate sensing noise, including thermal noise and residual clutter returns from non-target scatterers. In monostatic operation, self-interference is suppressed using a cancellation technique [12], then the residual leakage is absorbed into $\mathbf{z}(t)$. Finally, only one beam is used per sensing slot, avoiding inter-beam interference.

B. Environment Reconstruction Model

For each transmit beam direction (ϕ_i, θ_j) , the corresponding received signal $\mathbf{y}_n(t)$ is processed to estimate the round-trip time delay $\tau_{i,j}$ using conventional matched filtering approach [4]:

$$\tilde{\tau}_{i,j} = \arg\max_{\tau} \left| \int_0^{\Delta T_e} \mathbf{y}_n(t) \, s_n^*(t-\tau) \, dt \right|^2, \tag{4}$$

where ΔT_e denotes the observation window. The estimated propagation distance is then calculated as

$$\tilde{d}_{i,j} = \frac{c\,\tilde{\tau}_{i,j}}{2} = d_{i,j} + \epsilon_{i,j},\tag{5}$$

¹Each codebook beam is a unit-norm steering vector with identical mainlobe gain across angles, making direction-dependent gain variation negligible under single-beam probing. Moreover, the combination of directional beamforming, outdoor mmWave propagation, and wideband diversity ensures that the LoS path dominates in our system. where c is the speed of light and $\epsilon_{i,j} \sim \mathcal{N}(0,(\sigma_{i,j}^d)^2)$ with noise variance $(\sigma_{i,j}^d)^2$ is estimation error of $d_{i,j}$. Repeating this procedure across all beam directions (ϕ_i,θ_j) in \mathcal{B} yields an estimated distance matrix $\tilde{\Omega} = \{\tilde{d}_{i,j}\} \in \mathbb{R}^{W \times H}$. This distance matrix (DM) can be mapped into 3D Cartesian coordinates to form a coarse point cloud expressed as

$$\tilde{\mathbf{P}} = \{\mathbf{p}_{i,j}\} \in \mathbb{R}^{3 \times W \times H}, \quad \mathbf{p}_{i,j} = \tilde{d}_{i,j} \begin{bmatrix} \cos \theta_j \cos \phi_i \\ \cos \theta_j \sin \phi_i \\ \sin \theta_j \end{bmatrix}, \quad (6)$$

which provides an initial reconstruction of the surrounding environment. However, the estimated point cloud from the sensing process suffers from two key limitations: high noise variance of distance estimation and insufficient spatial sampling. In particular, both are related to the low SNR, long distance, and limited bandwidth in ISAC systems. Based on the received signal model in Eq. (3), the SNR corresponding to (ϕ_i, θ_j) is given by

$$\gamma_{i,j} = \frac{\mathbb{E}\left\{ \left\| \sqrt{N_t^2 N_r^2} \ g_{i,j} \ \mathbf{a}(\phi_i, \theta_j) \mathbf{a}^H(\phi_i, \theta_j) \ s_n(t - \tau_{i,j}) \right\|^2 \right\}}{\mathbb{E}\{ \left\| \mathbf{z}(t) \right\|^2 \}}$$

$$N_t^2 N^2 |\beta_{i,j}|^2 P_2 = N_t^2 N^2 \rho^2 P_2$$

$$= \frac{N_t^2 N_r^2 |\beta_{i,j}|^2 P_s}{\sigma_z^2} = \frac{N_t^2 N_r^2 \varrho^2 P_s}{4 d_{i,j}^2 \sigma_z^2}.$$

To characterize the uncertainty in the estimated distance $\tilde{d}_{i,j}$, we approximate the distance estimation error variance using the Cramér–Rao bound (CRB) [2], which sets a theoretical lower bound on the variance of unbiased estimators. Then, the noise variance of the distance estimation error is given by [2]

$$(\sigma_{i,j}^d)^2 = \alpha \text{ CRB}_{i,j} = \frac{\alpha c^2}{8\pi^2 \gamma_{i,j} B^2},$$
 (8)

where B is the effective bandwidth, and $\alpha \geq 1$ is a scaling factor that accounts for estimator efficiency. In practice, the variance inflation factor is typically bounded as $1 \leq \alpha \leq 2$, and seldom exceeds this range in radar and communication estimation problems [13]. In addition to degraded accuracy, the point cloud suffers from missed detections [14], leading to sparsely populated reconstructions. The detection probability of reflection point corresponding to (ϕ_i, θ_j) is derived by Marcum Q-function as follow [15]

$$P_{i,j} = Q_1 \left(\sqrt{2\gamma_{i,j}}, \sqrt{2\lambda} \right)$$

$$= \int_{\sqrt{2\lambda}}^{\infty} x \exp\left(-\frac{x^2 + 2\gamma_{i,j}}{2} \right) I_0 \left(x\sqrt{2\gamma_{i,j}} \right) dx,$$
(9)

where $I_0(\cdot)$ is the modified Bessel function of the first kind and zero order. Here, λ denotes the normalized detection threshold, which is chosen to satisfy a predefined false-alarm probability $P_{\rm FA}$ under the Neyman–Pearson criterion, i.e., $\lambda = -\ln P_{\rm FA}$ for single noncoherent detection [15].

At the single-beam level, the estimate $d_{i,j}$ is affected by additive noise and potential missed detection, with variance approximated by the CRB in Eq. (8) and detection probability $P_{i,j}$ given by the Marcum-Q function in Eq. (9). Extending this to the system level, when the BS performs beam sweeping over the codebook \mathcal{B} , these statistical

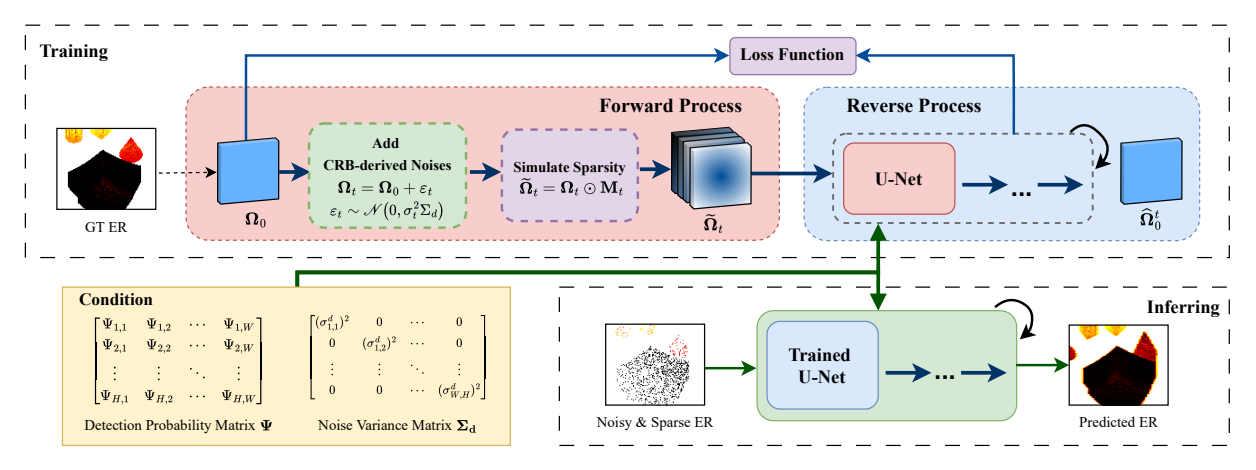


Fig. 2: Overview of the proposed NSADM framework.

characteristics are preserved across all directions (ϕ_i, θ_j) . Thus, the estimated DM $\tilde{\mathbf{\Omega}}$ inherits two degradation mechanisms: (i) Gaussian errors with variance matrix $\mathbf{\Sigma}_d = \mathrm{diag}\left((\sigma_{1,1}^d)^2, (\sigma_{1,2}^d)^2, \ldots, (\sigma_{W,H}^d)^2\right) \in \mathbb{R}^{WH \times WH}$ and (ii) missed detections governed by the probability matrix $\mathbf{\Psi} = \{P_{i,j}\} \in \mathbb{R}^{W \times H}$. This yields the compact representation

$$\tilde{\mathbf{\Omega}} = (\mathbf{\Omega} + \epsilon) \odot \mathbf{M},\tag{10}$$

where Ω denotes the ground-truth DM, $\epsilon \sim \mathcal{N}(0, \Sigma_d)$ models CRB-based errors, and $\mathbf{M} = [M_{i,j}] \in \{0,1\}^{W \times H}$ is a random mask with $\Pr(M_{i,j} = 1) = \Psi_{i,j}, \forall (i,j)$.

C. Problem Formulation

In this letter, we investigate ER in ISAC, whose performance depends on the fidelity of the estimated DM $\tilde{\Omega}$. Therefore, our objective is to design a mapping function $\mathcal{F}(\cdot)$ that refines the coarse and noisy estimation $\tilde{\Omega}$ into a more accurate and dense DM $\hat{\Omega}$, which can then be used to reconstruct the 3D environment. Additionally, we incorporate the CRB-based noise variance map Σ_d and the detection probability map Ψ as auxiliary inputs. The resulting optimization problem is formulated as

$$\min_{\mathcal{F}} \mathcal{L}(\widehat{\Omega}, \Omega), \quad \widehat{\Omega} = \mathcal{F}(\widetilde{\Omega}, [\Psi, \Sigma_d])
\text{s.t. } \frac{1}{WH} \|\Psi\|_1 \geq \rho_0, \quad \frac{1}{WH} \operatorname{tr}(\Sigma_d) \leq \sigma_0^2,$$
(11)

where $\mathcal{L}(\cdot)$ measures the geometric discrepancy between the predicted and ground-truth distance matrices. To ensure realistic reconstruction conditions, we impose a minimum average detection probability ρ_0 to guarantee sufficient geometric coverage and an upper bound on the average noise variance σ_0^2 to limit estimator uncertainty. Eq. (11) constitutes a high-dimensional and ill-posed inverse problem [16]–[18]. To address this challenge, we propose a *NSADM* model that leverages the CRB-based noise variance matrix and the detection probability matrix to guide the reconstruction process [19].

III. NSADM: Noise-Sparsity-Aware Diffusion Model-Based Point Cloud Enhancement

Fig. 2 illustrates the overall architecture of the NSADM framework. During training, the forward process sequentially injects CRB-based anisotropic noise and simulates beam-dependent sparsity. The reverse process then exploits the noise variance matrix Σ_d and detection probability matrix Ψ as conditioning information to denoise and densify the corrupted

DM. The details of the proposed framework are discussed in the following subsections.

A. Noise-Sparsity-Aware Forward Process

We adopt a score-based generative model (SGM) [11] because it allows customizable noise covariance, unlike traditional denoising diffusion probabilistic models that inject isotropic Gaussian noise. This enables us to model the CRB-based anisotropic characteristics of ISAC measurements, where different beam directions exhibit different noise levels. Specifically, the forward process perturbs the clean data using an anisotropic Gaussian distribution governed by the CRB-based noise matrix Σ_d under a sequence of increasing noise levels $0 < \sigma_1 < \sigma_2 < \cdots < \sigma_T$. Starting from the ground-truth DM Ω_0 , the corrupted sample at timestep t is drawn as

$$q(\mathbf{\Omega}_t \mid \mathbf{\Omega}_0) = \mathcal{N}\left(\mathbf{\Omega}_t; \mathbf{\Omega}_0, \, \sigma_t \widehat{\mathbf{\Sigma}}_d\right), \quad \widehat{\mathbf{\Sigma}}_d = \frac{WH}{\operatorname{tr}(\mathbf{\Sigma}_d)} \, \mathbf{\Sigma}_d$$
(12)

where σ_t is the noise level at timestep t, and $\widehat{\Sigma}_d$ is the normalized CRB-based variance matrix Σ_d .

In addition to noise, ISAC reconstructions suffer from sparse detections due to limited SNR and thresholding effects. To model this, we construct a detection probability matrix $\Psi \in [0,1]^{W \times H}$, where $\Psi(i,j)$ denotes the probability of detecting a reflection in beam direction (ϕ_i,θ_j) as defined in Sec. II-B. Based on Ψ , we generate a binary sampling mask $\mathbf{M}_t \in \{0,1\}^{W \times H}$ following a sampling schedule $\rho_t \in [0,1]$ that controls the proportion of retained points at step t:

$$\mathbf{M}_{t}(i,j) = \begin{cases} 1, & \text{if } \rho_{t} \ \mathbf{\Psi}(i,j) > \mu, \quad \mu \sim \mathcal{U}(0,1), \\ 0, & \text{otherwise.} \end{cases}$$
 (13)

Applying this mask to the noisy DM yields $\tilde{\Omega}_t = \mathbf{M}_t \odot \Omega_t$. This step enforces sparsity consistent with ISAC detection statistics and produces the degraded input $\tilde{\Omega}_t$ used by the reverse denoising process.

B. Noise-Sparsity-Conditioned Reverse Process

In SGMs, the reverse process iteratively denoises the corrupted sample by approximating the posterior transition $p(\Omega_{t-1} | \Omega_t)$. We augment this process by conditioning on $\mathbf{C} = \{\Psi, \widehat{\Sigma}_d\}$, which encode detection probability and noise variance, respectively. This conditioning reduces posterior



Fig. 3: Qualitative comparison of point cloud reconstruction across two representative scenes. From left to right: Ground Truth, initial ISAC estimation, Proposed NSADM, DIPR [23], DnCNN [24], and MT [25]. The darker colors indicate closer distances to the BS, while lighter colors represent farther points.

uncertainty, as quantified by conditional mutual information:

$$I(\Omega; \mathbf{C} \mid \tilde{\Omega}) = H(\Omega \mid \tilde{\Omega}) - H(\Omega \mid \tilde{\Omega}, \mathbf{C}) \ge 0,$$
 (14)

where $H(\cdot)$ denotes Shannon entropy [20]. The conditional reverse transition is

$$p_{\theta}(\mathbf{\Omega}_{t-1} \mid \mathbf{\Omega}_t, \mathbf{C}) = \mathcal{N}\left(\mathbf{\Omega}_{t-1}; \mu_{\theta}(\mathbf{\Omega}_t, t, \mathbf{C}), \sigma_t^2 \widehat{\mathbf{\Sigma}}_d\right),$$
 (15)

where μ_{θ} is the learned conditional mean. Following Karras et al. [21], we employ a denoising network $R_{\rm w}(\cdot)$ to directly predict the clean DM:

$$\widehat{\mathbf{\Omega}}_0^t = R_{\mathbf{w}}(\mathbf{\Omega}_t, t, \mathbf{C}), \tag{16}$$

which has been shown to improve training stability.

C. Objective Function

Training the NSADM framework is guided by a hybrid loss that balances numerical accuracy with structural consistency. The total loss is defined as

$$\mathcal{L}_{\text{total}} = \underbrace{\left\| \mathbf{\Omega}_0 - \widehat{\mathbf{\Omega}}_0^t \right\|_2^2}_{\text{MSE Loss}} + \lambda \underbrace{\left\| f(\mathbf{\Omega}_0) - f(\widehat{\mathbf{\Omega}}_0^t) \right\|_2^2}_{\text{Perceptual Loss}}, \tag{17}$$

where $f(\cdot)$ is a fixed feature extractor which is pretrained to capture generic structural patterns such as edges and contours, and λ controls the trade-off between fidelity and perceptual quality.

The first term is a mean squared error (MSE) loss, which penalizes deviations in per-beam distance estimation in regions where reliable measurements exist. However, MSE operates solely in pixel space and tends to oversmooth reconstructions, particularly in sparse or noisy areas. To complement this, we incorporate a perceptual loss based on the Learned Perceptual Image Patch Similarity (LPIPS) metric [22], which leverages $f(\cdot)$ to preserve global structural consistency that cannot be enforced by MSE alone.

D. Training and Inference

During training, the model predicts the ground-truth DM at each diffusion step using the hybrid loss in Eq. (17). At inference, the model takes the degraded DM $\tilde{\Omega}$ and applies the conditional reverse process in Eq. (16). Each step refines the estimate by denoising and densifying under the guidance of Ψ and $\hat{\Sigma}_d$. After T iterations, the final DM $\hat{\Omega}$ is mapped to 3D Cartesian coordinates to produce the point cloud $\hat{\mathbf{P}}$.

The computational complexity follows that of standard CNN-based diffusion models. As discussed in Karras et al. [21], each denoising step is dominated by convolutional operations over a feature map of size $H \times W$ with N_c channels, leading to a per-step cost of $\mathcal{O}(N_cHW)$. Therefore, the overall inference complexity scales linearly with the number of sampling steps T, resulting in a total cost of $\mathcal{O}(TN_cHW)$.

IV. EXPERIMENTAL RESULTS

A. Dataset Generation and Benchmark Selection

To evaluate the performance of the proposed framework, we generate a synthetic ISAC dataset of 1,000 outdoor-like scenes using a simulation pipeline implemented in Python3.11 with standard scientific libraries. Each scene is constructed using a 3D mesh engine, where multiple objects with varying shapes and RCS values are randomly placed within a 30 m sensing radius. A monostatic BS, positioned at a height of 20-25 m and equipped with a 4×4 UPA, scans over a predefined azimuth-elevation codebook. The system operates with a 1 GHz bandwidth and a noise power of -20 dBm. Echo generation and range estimation follow the signal and processing models in Sec.II-A and Sec.II-B, producing noisy distance matrices that are then mapped to Cartesian coordinates to form point clouds. The dataset is finally partitioned into training, validation, and testing subsets. All experiments are performed on an NVIDIA GeForce RTX3090 GPU with an AMD EPYC 7313 16-core processor. Benchmark comparisons include morphological transformation (MT) [25], DnCNN [24], and DPIR [23], representing classical model-based, discriminative learning-based, and diffusion-prior-based methods respectively.

B. Performance Evaluation

- 1) Qualitative Comparison: Fig. 3 presents a qualitative comparison, showing that the proposed NSADM framework outperforms all baselines by jointly achieving effective densification and strong denoising, producing clear object boundaries and structurally consistent scenes. DnCNN only partially suppresses noise and fails to recover missing structures, yielding blotchy artifacts due to its single-pass design, while our iterative approach with CRB-guided noise injection handles anisotropic ISAC noise more effectively. DPIR offers stronger noise suppression through diffusion priors and iterative refinement, generating visually sharper outputs. However, the lack of perceptual loss leads to weak geometric fidelity, with noticeable shape deformation such as rounded corners and misaligned edges. MT, while able to interpolate gaps when neighbors exist, lacks denoising capability and fails in highly sparse areas, producing distorted or incomplete shapes. Under very low SNR, the high missed detection probability causes all methods, including NSADM, to produce incomplete reconstructions or spurious objects [26]-[28]. Addressing this fundamental challenge is a key direction for future work.
- 2) Quantitative Comparison: We evaluate using RMSE for point-wise accuracy and Chamfer Distance (CD) for global geometric alignment. While RMSE directly corresponds to the MSE training term, CD indirectly benefits from the perceptual

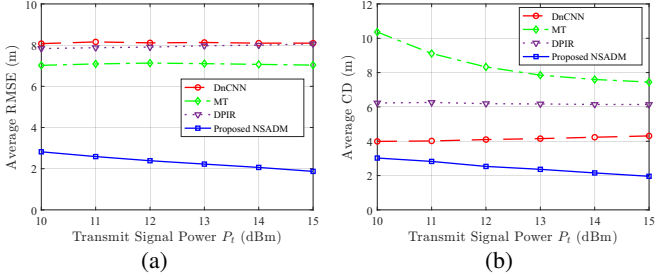


Fig. 4: Performance comparison of NSADM, DnCNN, and MT in terms of (a) average RMSE and (b) average CD across varying transmit powers.

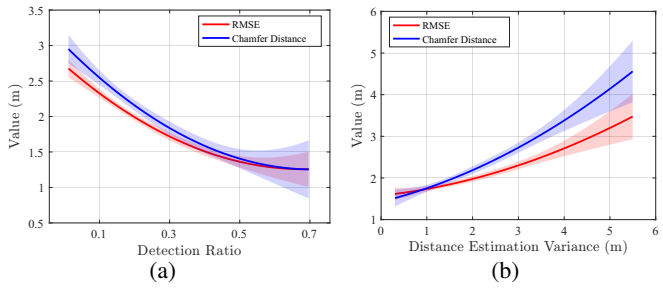


Fig. 5: Illustration of correlation between (a) detection ratio and (b) noise variance with average RMSE and CD.

loss, which enforces structural coherence in estimated distance matrices. The CD is given by

$$CD(\widehat{\mathbf{P}}, \mathbf{P}) = \frac{1}{|\widehat{\mathbf{P}}|} \sum_{x \in \widehat{\mathbf{P}}} \min_{y \in \mathbf{P}} \|x - y\|_2^2 + \frac{1}{|\mathbf{P}|} \sum_{y \in \mathbf{P}} \min_{x \in \widehat{\mathbf{P}}} \|y - x\|_2^2.$$
(18)

CD aggregates bidirectional nearest-neighbor distances, making it sensitive to missing regions and outliers. Fig. 4 reports average RMSE and CD across all test scenes under varying transmit powers. NSADM achieves the lowest errors across all conditions, reducing RMSE by over 60% and CD by over 50% compared to the strongest baseline, which is MT and DnCNN, respectively. DnCNN exhibits nearly constant performance across different powers, reflecting its limited sensitivity to SNR and its local denoising mechanism. MT improves slightly as power increases but remains unreliable in sparse regions due to its dependence on neighboring reflections. DPIR performs better than DnCNN in dense areas owing to its diffusion priors, yet still introduces geometric distortions since it lacks ISACspecific physical constraints. In contrast, NSADM's errors decrease consistently with transmit power, demonstrating the effectiveness of its CRB-guided noise-sparsity-aware formulation.

3) Correlation Analysis: Fig. 5 examines how detection ratio and noise variance affect reconstruction fidelity. Both RMSE and CD decrease as detection ratio increases, with graceful degradation even under severe sparsity. Notably, the degradation is relatively modest across detection ratios from 5% to 70%, demonstrating the robustness to extreme undersampling. Conversely, both metrics increase nearly linearly with noise variance, reflecting expected fidelity loss under higher measurement uncertainty. CD exhibits higher sensitivity than RMSE in both cases, particularly under high noise conditions, suggesting that geometric alignment degrades faster

than point-wise accuracy when measurement quality deteriorates. These results confirm that NSADM maintains consistent performance across diverse sparsity and noise conditions.

V. Conclusion

This letter presented NSADM, a diffusion-based framework for refining sparse and noisy ISAC-enabled point clouds. By modeling CRB-based noise and detection sparsity, the method aligns the denoising process with ISAC-specific degradations, yielding denser and more structurally accurate reconstructions. Experiments across varying transmit powers demonstrate consistent gains over learning-based and interpolation baselines. Future work will extend the framework to dynamic scenarios and explore adaptive sensing strategies.

REFERENCES

- Q. D. M. Nguyen, W. D. Lukito, X. Liu, and C. Liu, "Deep Learning-Empowered RF Sensing in Outdoor Environments: Recent Advances, Challenges, and Future Directions," *Electronics*, vol. 14, no. 1, p. 125, 2024
- [2] A. Liu, Z. Huang, M. Li, Y. Wan, W. Li, T. X. Han, C. Liu, R. Du, D. K. P. Tan, J. Lu, Y. Shen, F. Colone, and K. Chetty, "A Survey on Fundamental Limits of Integrated Sensing and Communication," *IEEE Commun. Surv. Tutor.*, vol. 24, no. 2, pp. 994–1034, 2022.
- [3] C. Liu, S. Li, W. Yuan, X. Liu, and D. W. K. Ng, "Predictive precoder design for OTFS-enabled URLLC: A deep learning approach," *IEEE J. Sel. Areas Commun.*, vol. 41, no. 7, pp. 2245–2260, Jul. 2023.
- [4] C. Liu, W. Yuan, S. Li, X. Liu, H. Li, D. W. K. Ng, and Y. Li, "Learning-based predictive beamforming for integrated sensing and communication in vehicular networks," *IEEE J. Sel. Areas Commun.*, vol. 40, no. 8, pp. 2317–2334, Aug. 2022.
- [5] W. Yuan, C. Liu, F. Liu, S. Li, and D. W. K. Ng, "Learning-based predictive beamforming for UAV communications with jittering," *IEEE Wireless Commun. Lett.*, vol. 9, no. 11, pp. 1970–1974, Nov. 2020.
- [6] A. Bazzi, M. Ying, O. Kanhere, T. S. Rappaport, and M. Chafii, "ISAC Imaging by Channel State Information Using Ray Tracing for Next-Generation 6G," *IEEE J. Sel. Topics Electromagn.*, Antennas Propag., 2025.
- [7] B. Lin, C. Zhao, F. Gao, G. Y. Li, J. Qian, and H. Wang, "Environment Reconstruction Based on Multi-User Selection and Multi-Modal Fusion in ISAC," *IEEE Trans. Wireless Commun.*, vol. 23, no. 10, pp. 15083– 15095, 2024.
- [8] C. Liu, W. Yuan, Z. Wei, X. Liu, and D. W. K. Ng, "Location-aware predictive beamforming for UAV communications: A deep learning approach," *IEEE Wireless Commun. Lett.*, vol. 10, no. 3, pp. 668–672, Mar. 2021
- [9] C. Liu, X. Liu, S. Li, W. Yuan, and D. W. K. Ng, "Deep clstm for predictive beamforming in integrated sensing and communicationenabled vehicular networks," *Journal of Communications and Informa*tion Networks, vol. 7, no. 3, pp. 269–277, 2022.
- [10] B. Lu, Z. Wei, H. Wu, X. Zeng, L. Wang, X. Lu, D. Mei, and Z. Feng, "Deep-Learning-Based Multinode ISAC 4D Environmental Reconstruction With Uplink–Downlink Cooperation," *IEEE Internet Things J.*, vol. 11, no. 24, pp. 39512–39526, 2024.
- [11] L. Yang, Z. Zhang, Y. Song, S. Hong, R. Xu, Y. Zhao, W. Zhang, B. Cui, and M.-H. Yang, "Diffusion Models: A Comprehensive Survey of Methods and Applications," ACM Comput. Surv., vol. 56, no. 4, Nov. 2023
- [12] E. Ahmed and A. M. Eltawil, "All-digital self-interference cancellation technique for full-duplex systems," *IEEE Trans. Wireless Commun.*, 2015.
- [13] P. Stoica, X. Shang, and Y. Cheng, "The Cramér-Rao Bound for Signal Parameter Estimation from Quantized Data," *IEEE Signal Process. Mag.*, vol. 39, no. 1, pp. 118–125, 2022.
- [14] C. Liu, H. Li, and M. Jin, "Blind central-symmetry-based feature detection for spatial spectrum sensing," *IEEE Trans. Veh. Technol.*, vol. 65, no. 12, pp. 10147–10152, Dec. 2016.
- [15] D. A. Shnidman, "Radar Detection Probabilities and Their Calculation," IEEE Trans. Aerosp. Electron. Syst., vol. 31, no. 3, pp. 928–950, 2002.
- [16] C. Liu, X. Liu, D. W. K. Ng, and J. Yuan, "Deep residual learning for channel estimation in intelligent reflecting surface-assisted multi-user communications," *IEEE Trans. Wireless Commun.*, vol. 21, no. 2, pp. 898–912, Feb. 2022.

- [17] C. Liu, Z. Wei, D. W. K. Ng, J. Yuan, and Y.-C. Liang, "Deep transfer learning for signal detection in ambient backscatter communications," *IEEE Trans. Wireless Commun.*, vol. 20, no. 3, pp. 1624–1638, Mar. 2021.
- [18] X. Liu, C. Liu, Y. Li, B. Vucetic, and D. W. K. Ng, "Deep residual learning-assisted channel estimation in ambient backscatter communications," *IEEE Wireless Commun. Lett.*, vol. 10, no. 2, pp. 339–343, Feb. 2021.
- [19] C. Liu, X. Liu, Z. Wei, D. W. K. Ng, and R. Schober, "Scalable predictive beamforming for IRS-assisted multi-user communications: A deep learning approach," arXiv preprint arXiv:2211.12644, 2022.
- [20] Y. Wang, Y. Schiff, A. Gokaslan, W. Pan, F. Wang, C. D. Sa, and V. Kuleshov, "InfoDiffusion: Representation Learning Using Information Maximizing Diffusion Models," in *Proc. Int. Conf. Mach. Learn.* (ICML). PMLR, 2023, pp. 36336–36354.
- [21] T. Karras, M. Aittala, T. Aila, and S. Laine, "Elucidating the Design Space of Diffusion-Based Generative Models," *Adv. Neural Inf. Process.* Syst., vol. 35, pp. 26565–26577, Dec. 2022.
- [22] R. Zhang, P. Isola, A. A. Efros, E. Shechtman, and O. Wang, "The Unreasonable Effectiveness of Deep Features as a Perceptual Metric,"

- in Proc. IEEE Conf. Comput. Vis. Pattern Recognit. (CVPR), 2018, pp. 586-595.
- [23] K. Zhang, Y. Li, W. Zuo, L. Zhang, L. V. Gool, and R. Timofte, "Plug-and-play image restoration with deep denoiser prior," *IEEE Trans. Pattern Anal. Mach. Intell.*, 2021.
- [24] K. Zhang, W. Zuo, Y. Chen, D. Meng, and L. Zhang, "Beyond a Gaussian denoiser: Residual learning of deep CNN for image denoising," *IEEE Trans. Image Process.*, vol. 26, no. 7, pp. 3142–3155, 2017.
- [25] K. Sreedhar and B. Panlal, "Enhancement of images using morphological transformations," *Int. J. Comput. Sci. Inf. Technol.*, vol. 4, no. 1, pp. 33–50, 2012.
- [26] C. Liu, J. Wang, X. Liu, and Y.-C. Liang, "Deep CM-CNN for spectrum sensing in cognitive radio," *IEEE J. Sel. Areas Commun.*, vol. 37, no. 10, pp. 2306–2321, Oct. 2019.
- [27] —, "Maximum eigenvalue-based goodness-of-fit detection for spectrum sensing in cognitive radio," *IEEE Trans. Veh. Technol.*, vol. 68, no. 8, pp. 7747–7760, Aug. 2019.
- [28] C. Liu, H. Li, J. Wang, and M. Jin, "Optimal eigenvalue weighting detection for multi-antenna cognitive radio networks," *IEEE Trans. Wireless Commun.*, vol. 16, no. 4, pp. 2083–2096, Apr. 2017.